Photofragment imaging by sections for measuring state-resolved angle-velocity differential cross sections

Jack A. Syage
The Aerospace Corporation, P.O. Box 92957, M5-754, Los Angeles, California 90009

(Received 8 February 1996; accepted 3 April 1996)

We describe a two-dimensional (2D) imaging technique for recording state-specific photofragment angle-velocity (θ,v) distributions. In these experiments the photofragment images are recorded as 2D sections of the 3D angular distributions using state-specific ionization in a time-of-flight mass spectrometer. We compare this method to previous methods that record 2D projections of the 3D distribution. The 2D sections represent cartesian flux-velocity maps in the center of mass and are related to angle-velocity differential cross sections by a simple geometric factor. Two studies are highlighted. In the first, new results are presented for the A state photodissociation of CH_3I to CH_3+I. (θ,v) images are presented for I atom in the $^2P_{3/2}$ and $^2P_{1/2}$ spin–orbit states following photodissociation at 266 and 304 nm. The principal result is detection of the weak perpendicular transitions to the $^3Q_1$ state (at 304 nm) and the ^1Q state (at 266 nm) that underlie the strong parallel transition to the $^3Q_0$ state. We also report the ratio of cross sections $\sigma_\perp/\sigma_\parallel$, the anisotropy and branching ratio for I($^2P_{3/2}$) and I($^2P_{1/2}$), and the $^3Q_0$–^1Q surface crossing probability. In a second study the photodissociation of O_3 to $O_2(v)$+O($^3P_{j=2,1,0}$) was measured. A bimodal anisotropic velocity distribution was measured for O(^3P) corresponding to maximum in the $O_2(v)$ vibrational distribution of $v=15$ and 27, in general agreement with a previous measurement. The anisotropies of the high- and low-velocity components were measured to be $\beta\approx1.1$ and 0.4, respectively. © *1996 American Institute of Physics.* [S0021-9606(96)01526-7]

I. INTRODUCTION

The field of experimental chemical dynamics is based on measuring detailed properties of reactants and products from which potential energy surfaces can be determined. Many strategies have been developed to acquire this information. Recent ultrafast experiments that probe reactions on timescales less than the collision and dissociation time are providing direct information on potential energy surfaces.[1,2] Resonance Raman or emission spectroscopy of dissociating states provides detailed information on the dissociative surface.[3] These methods use optical transitions to directly probe regions of the dissociative potential energy surface. In effect they probe the difference potential between the two surfaces involved in the transition. An alternative approach to probing reactive surfaces is to measure state-specific angle-velocity distributions of the final products.[4,5] Though considered an indirect method, it has proven capable of revealing important details of potential energy surfaces and has the advantage of probing regions that might be optically inaccessible.[6,7] This paper is concerned with the latter approach. Many techniques have been developed over the years. Here we describe a method that records complete mappings of state-resolved differential cross sections with respect to angle and velocity. In this paper we present results for photodissociation reactions; however, the technique is also applicable to bimolecular reactive scattering in the gas phase, in photo-initiated van der Waals aligned complexes, and on surfaces.

The traditional method for measuring photofragment angle-velocity distributions is by translational energy spectroscopy introduced by Wilson and co-workers[8] and refined by Lee and co-workers.[9] A molecular beam is crossed by a photodissociation laser and the product angle-velocity distributions are measured in the laboratory frame using a rotating mass spectrometer. Alternatively, the photolysis laser polarization can be rotated and product detected using a fixed mass spectrometer. Photofragment translational energy spectroscopy offers superior angle and velocity resolution; however, data collection is time consuming, products are not detected in specific rovibrational energy states, and a transformation is required to convert from lab frame to center of mass frame differential cross sections. Variants of this technique for obtaining product state-specificity involve resonance ionization of product in the photolysis region[10] and more recently the powerful technique of resonant high-n Rydberg excitation and field ionization at the detector.[11,12] However, care must be taken to prevent Doppler selection by the probe laser from influencing the detected velocity distribution.

A popular method for measuring state-specific angle-velocity distributions is by polarized pump excitation followed by Doppler measurements of product recoil using polarized laser induced fluorescence detection.[13,14] These measurements provide vital information on vector correlations involving the velocity vectors, transition moment vectors and fragment angular momentum vectors. However, the velocity resolution is limited, particularly for heavy photofragments. Also accurate measurements of the anisotropy are difficult because the Doppler excitation spectra are typically recorded as 1D projections of the 3D distributions. To obtain more accurate angular information, Wittig and co-workers used delayed laser excitation to record a 1D core of the 3D distribution in a method called velocity-aligned Doppler

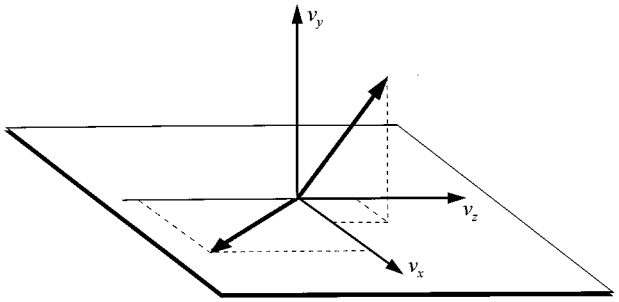

FIG. 1. Diagram illustrating 2D velocity measurements for detection in-plane (section) vs out-of-plane (projection).

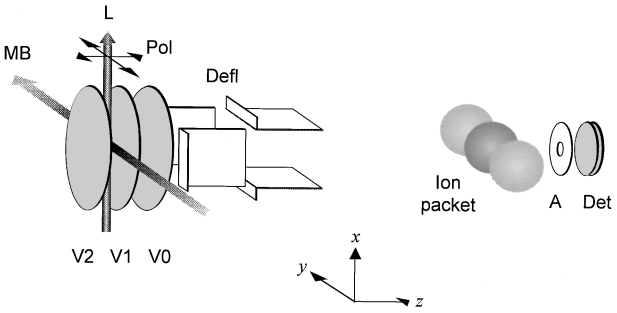

FIG. 2. Schematic diagram of the experiment. The molecular beam (MB) and laser (L) of polarization (Pol) cross perpendicularly in the acceleration region ($V0-V2$) of a TOF mass spectrometer. Deflector plates (Defl) center the ion packet across the aperture (A) placed in front of the detector (Det).

spectroscopy (VADS).[15] A related method for measuring state-specific angle-velocity distributions in a molecular beam is based on resonant ionization in a time-of-flight mass spectrometer (TOFMS).[16–18] Photofragment velocity is measured by the spread in the ion arrival time distribution. Angular specificity is obtained by recording a 1D core of the 3D distribution using an aperture at the detector.[18] Recently, the Zare group has reported on the use of core extraction for measuring state-to-state differential cross sections of bimolecular reactions.[19] In another-development, Zewail and coworkers are conducting femtosecond measurements using TOFMS fragment velocity measurements.[20]

2D photofragment imaging was pioneered by Chandler and Houston. This powerful technique has been demonstrated for isolated molecule photofragmentation[21,22] as well as for bimolecular reactive scattering.[23] 2D images of the 3D angle-velocity distribution are recorded on an intensified charge-coupled device (CCD) camera system placed at the end of a TOFMS. In this method all ions are collected; in effect the 3D distribution is flattened onto the plane of the detector in what is termed a 2D projection. Fragments having velocity vectors that are not parallel to the plane of the detector project onto the detector with velocity components less than their vectorial velocities. The true velocity or speed distribution is obtained by inverting the 2D projection by an Abel transformation. Image reconstruction is a well-established mathematic algorithm. Still, it is sometimes desirable to have a technique that measures angle-velocity distributions directly. This can be achieved by recording a 2D image as a planar section of the 3D distribution. The concept is to collect only fragments that recoil nearly in a single plane as illustrated in Fig. 1. By avoiding the velocity projection of fragments that lie out of the detection plane, the true velocity distribution is measured directly. The only transformation required is a simple linear Jacobian function that relates solid angle of detection to velocity. Adaptations to achieve 2D sections by the Chandler and Houston method have been proposed. Kinugawa and Arikawa used Doppler selection to ionize only photofragments that recoil in the plane of the detection.[24] However, this method imposes constraints on the position of the laser relative to the drift tube axis. Also Doppler selection is limited by the bandwidth of the laser and by the velocity spread of the photofragments, which can be very small for heavy fragments. Tonokura and Suzuki ionized a 2D photofragment slice by allowing the photofragment packet to expand and then ionizing with a sheet of laser light.[25] This interesting technique has the constraint that the size of the expanded photofragment packet is limited by the intensity of light needed to achieve multiphoton ionization and by the requirement of a very homogeneous intensity profile across the sheet. Finally, we mention two different proposals for achieving state-specific angle-velocity measurements of photodissociation using LIF imaging.[26,27]

In this paper, we describe a two-dimensional imaging technique for recording state-specific photofragment angle-velocity (θ,v) distributions.[28,29] In these experiments the photofragment images are recorded as 2D sections of the 3D angular distributions using state-specific ionization in a time-of-flight mass spectrometer. The technique is demonstrated using as examples new results for two molecular systems; (1) the A state photodissociation of CH_3I to $CH_3+I(^2P_{3/2,1/2})$ and (2) the photodissociation of O_3 to $O_2(v)+O(^3P_{j=2,1,0})$. Variants of the present technique have also been used to measure state-specific angle-velocity distributions for photoproducts escaping van der Waals dimers and clusters.[30] For photoinitiated dimer reactions, one obtains state-resolved differential cross sections for bimolecular reactive scattering.

II. EXPERIMENTAL METHOD

A. Instrumentation

The experimental method of recording 2D sectional or planar images is illustrated in Fig. 2. Photodissociation is initiated and products are ionized in a molecular beam TOF mass spectrometer. The ionized photofragment distribution is injected into a drift tube where it travels field-free toward a microchannel plate detector (MCP). The expanding ion packet represents the 3D photofragment velocity distribution. An aperture is placed in front of the detector to limit detection of the 3D ion distribution to a narrow cylinder of ions. The resultant measurement is a 1D ''core-sampled'' TOF spectra. The concept of ''core-sampling'' (sometimes referred to as core extraction) is to record a TOF spectrum in which the velocity distribution along the drift-tube axis is measured while limiting the velocities along the orthogonal

directions to a very small range. The aperture functions in that capacity. This concept is explored in more detail shortly (Sec. IV B).

A 2D planar velocity distribution is obtained by rastering the ion packet across the detection aperture using deflector plates and recording a 1D core TOF spectra at each position. Velocity is measured along the z axis by the TOF distribution and along the x-or y axis by spatial deflection of the ion packet. The relations are given by

$$v_z = \frac{qF(t-t_0)}{m} \tag{1}$$

$$v_{x,y} = \frac{l}{t_0} = \frac{KV_{x,y}}{t_0}. \tag{2}$$

Equation (1) represents two-stage acceleration under space focusing conditions, where F is the extraction field, q is charge, m is mass, and $t-t_0$ is the arrival time relative to the center of the distribution. In Eq. (2), K is a constant relating the deflection voltage $V_{x,y}$ to the spatial deflection l at the detector. Space focusing conditions[31] are obtained by first calculating the proper ratio of extraction to acceleration voltage $R=(V2\text{-}V1)/V1\text{-}V0)$, and then moving the position of the ionization volume along the z axis and monitoring the change in the ion TOF. R is adjusted by varying $V1$ until the ion TOF is insensitive to initial position. The optimized value of R is within 10% of the calculated value.

Our TOFMS consists of an ion optics assembly of three grids separated by 1 cm, a 1 m drift tube, and a 5 mm diam aperture mounted in front of an 18 mm diam MCP. To improve velocity resolution at the detector, extraction and acceleration fields are minimized in order to maximize the time available for the ion packet to expand. For a low velocity fragment, such as I in CH_3I photodissociation, we typically used extraction and acceleration fields of 15 and 230 V/cm, respectively, giving an ion drift time of $t_0=72$ μs and a maximum $t-t_0$ of about 1.2 μs.[28] For more energetic fragments, such as O atoms from O_3 photodissociation, we used extraction and acceleration fields of 20–30 V/cm and 300–500 V/cm, which give drift times ranging from about $t_0=14$–19 μs and a maximum $2(t-t_0)$ of about 0.5–1.0 μs.[29] Ion TOF spectra were collected by digitizing the MCP anode current using a LeCroy 9450 digital storage scope (CH_3I results) or by ion counting using a Stanford Research Systems SR 430 multichannel scalar/averager (O_3 results). The latter device is preferred because we usually operate at low count rates in order to avoid space charge repulsion.

We generally record about 10–20 one-dimensional TOF spectra to construct a 2D photofragment image. It is only necessary to record one-half of an image because of axial symmetry, in which case about 10 one-dimensional spectra suffice. A 1D TOF spectra takes about 1–2 min to collect (e.g., signal averaging over 2000 pulses at 20 Hz). Complete 2D images can be obtained in well under 30 min. The necessity of rastering the ion packet across the detector aperture and recording a series of 1D TOF spectra means that single-shot images are not obtained. In principal, single-shot images can be obtained by the 2D projection method that uses CCD detectors; however, in reality the ionizing laser must be scanned over the entire Doppler width of the product transition in order to build up a 2D projection that represents all ion velocities and angles. Our 2D sections technique, however, lends itself to recording single-shot images. A natural extension of our technique is to incorporate a MCP detector with a segmented anode array. Then the complete set of 1D TOF spectra that comprise a 2D image can be recorded simultaneously. A slit in front of the detector would restrict the detected photofragments to a single plane. We are considering a 32-channel anode array coupled to a 32-channel pipeline time-to-digital converter processing 8 hits per channel per pulse (e.g., LeCroy 3377, Sec. 7.1). Improving data collection efficiency by over an order of magnitude opens up the potential to record high sensitivity images of bimolecular chemical dynamics, scattering off of surfaces, and product recoil from clusters. Although signal averaging will still be necessary, a single-shot imaging method is preferred because it has better immunity to fluctuations and drifts in operating conditions than does a scanning method for recording images.

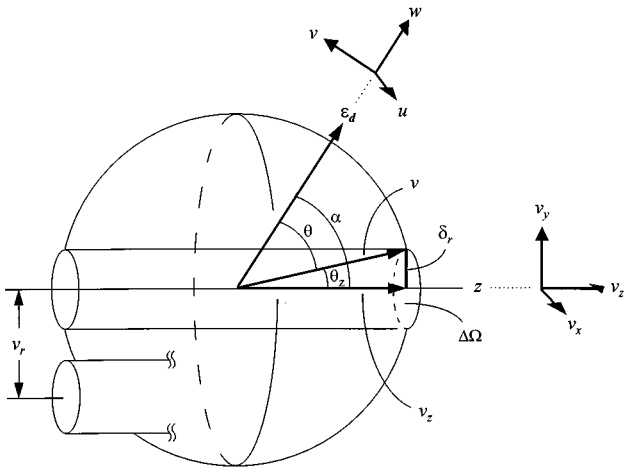

FIG. 3. Geometry for product recoil and detection cylinder. Parameters are described in the text. Also shown is the relationship between the space-fixed $v_x v_y v_z$ laboratory frame and the body-fixed uvw polarization frame.

Details on sample preparation for the two case studies, CH_3I and O_3 photodissociation, can be found elsewhere.[28–30]

B. Angle-velocity resolution

The detection geometry for measuring angle-resolved time-of-flight (TOF) spectra is illustrated in Fig. 3. The sphere in Fig. 3 represents a surface of ions of speed v. The detection aperture limits the field of view to a cylinder of ions of maximum radial velocity $\delta_r = r/t_0$ where r is the effective aperture radius, and t_0 is the ion packet drift time. The angular and velocity resolutions are dependent on photofragment speed v and are given by

$$\Delta\theta_z = \arcsin(\delta_r/v) \quad \text{(angular resolution)}, \tag{3}$$

$$\Delta v/v = 1-(v_{z,\min}/v) = 1-\cos\Delta\theta_z \quad \text{(velocity resolution)}. \tag{4}$$

The detection cylinder limits the angular range of fragment of velocity v, thereby limiting the width of the v_z projection. This defines the velocity resolution Δv. As δ_r decreases relative to v, the detected v_z distribution becomes a good measure of the speed distribution v. These concepts are developed mathematically in Sec. IV. In practice, the effective value of δ_r may be larger due to molecular beam velocity dispersion and to deflection of ions by small field periodicities at the grids (see Sec. VII). The actual instrument resolution is measured in the same manner as for photofragment velocity distributions, except that a parent molecule (i.e., no recoil velocity) is used. The radial velocity resolution is discussed in the context of specific photodissociation systems below. The size of the excitation volume has inconsequential effect on resolution since it is significantly smaller than the detector aperture size and the size of the ion packet that reaches the detector. The ion packet is allowed to expand to many times the size of the detector aperture in order to improve the core-sampling condition. This is in contract to 2D projection imaging in which the ion packet size must not exceed the size of the detector face.

III. VECTOR CORRELATIONS AND ALIGNMENT

We define a space-fixed laboratory frame and a molecular body-fixed polarization frame for velocity. The relationships are shown in Fig. 3. The laboratory velocity components v_x, v_y, v_z are defined relative to the drift tube z axis. The molecular velocity components u, v, w are defined relative to the dissociation-laser polarization (electric field) vector ϵ_d. The ϵ_d vector can rotate along the x axis through angle α relative to the laboratory z axis. Both the laboratory and molecular velocity components are in center-of-mass frames for dissociation. The c.m. polarization frame is useful because molecules align with ϵ_d by the transition moment vector μ ($\epsilon_d - \mu$ correlation). If dissociation is prompt then the correlation of the c.m. velocity vector ν with μ (v-μ correlation) probes the alignment of the μ relative to the molecular principal axis and bond breaking axis. This information can be valuable to assigning symmetries of excited electronic states.

Two sets of deflector plates along the x and y axis permit images to be recorded in either the xy or yz laboratory planes. The dissociation-laser polarization axis ϵ_d can be aligned along the z or y axis (denoted $\epsilon_d \| z$ and $\epsilon_d \perp z$ respectively) and serves to rotate the molecular frame. The combination of two laboratory planes of detection and two laser polarization alignments enables c.m. velocity measurements in four image planes (three orthogonal and one redundant) to be recorded. These combinations are tabulated in Table I. To illustrate the utility of measuring velocities in the body-fixed velocity planes, we consider CH_3I, which has a strong parallel and weak perpendicular transition moments relative to the principal C–I axis. To detect the parallel transition, one would probe for product recoil along the w direction (either the uw or vw plane, which are axially symmetric). To detect the perpendicular transition, one would probe for product recoil in the uv plane. Table I explains what set of experimental conditions are needed to measure these properties.

TABLE I. Relationship of velocity planes in the space-fixed laboratory frame and the molecular body-fixed polarization frame.

		Polarization frame	
	Laboratory frame	$\epsilon_d \| z$	$\epsilon_d \perp z$
x defl	$v_x v_z$	uw	uv
y defl	$v_y v_z$	vw	wv

We now relate the present TOF method to alignments and correlations observed by Doppler spectroscopy. The $\epsilon_d - \mu$ alignment is the same in both methods. The TOF detection axis z is analogous to the probe laser propagation vector (usually designated k_p) in Doppler spectroscopy. The probe laser polarization ϵ_p can be rotated in both Doppler and TOF measurements; however, the Doppler method is confined to $\epsilon_p \perp k_p$ whereas the TOF method allows both $\epsilon_p \perp z$ and $\epsilon_p \| z$ alignments. The latter capability is important for measuring $v - J$ correlations. One final comment comparing the merits of Doppler and TOF methods. The velocity resolution in the former method is limited by the laser bandwidth, therefore, the technique is most suited for low-mass fragments of relatively high velocity. This limitation does not exist for TOF spectra. Doppler and TOF spectra are often recorded as 1D projections (i.e., velocity-resolved along one axis and summed over the orthogonal components). The TOF 1D projection requires exciting over the entire Doppler width so that all velocity groups are sampled. This limitation requires narrow Doppler widths or a laser that is scanned over the Doppler line shape while accumulating a TOF spectrum. More detailed angle-velocity information is obtained by core sampling (i.e., velocity resolved for one component for some well-defined velocity components along the orthogonal directions). This can be achieved for the Doppler method using the VADS technique and for the TOF method using the core sampling technique (see Introduction). The TOF 1D-core sampling method views only a narrow velocity component range orthogonal to the drift-tube axis. This is a natural way to remove the narrow Doppler width limitation on the probe laser. In fact, if the probe laser propagates perpendicular to the drift-tube axis, as is typically the case, then narrow-band excitation can potentially improve core-sampling resolution by further narrowing the range of orthogonal velocity components that are detected in the TOF spectrum. Similarly, Doppler selected ionization can enhance the resolution of the 2D planar section perpendicular to the probe laser propagation axis, namely, the yz laboratory plane (Table I). For this reason, we prefer recording 2D images in the yz, rather than the xy plane. However, the latter plane is required if a photofragment image of a perpendicular angular distribution is needed, as discussed in Sec. V.

IV. MODEL FOR CARTESIAN FLUX MAPS AND DIFFERENTIAL CROSS SECTIONS

The intent of this section is to show the relation between the experimental photofragment maps and the angle-velocity

differential cross section. We also consider instrument resolution and discuss limits where the simple relations between the measurables and the differential cross sections break down.

A. General equations

The flux of ions along the z axis per unit time with radial velocity v_r is given by

$$\frac{d^2N}{dt\ dv_r} = \kappa \frac{d^2\sigma}{d\Omega\ dv}\left[\frac{d\Omega}{dv_z}\frac{dv_z}{dt}\frac{dv}{dv_r}\right] = \kappa \frac{d^2\sigma}{d\Omega\ dv}\left[\frac{-2\pi}{v}\frac{qF}{m}\frac{v_r}{v}\right]. \tag{5}$$

The evaluation of $d\Omega/dv_z$ follows from Fig. 3 and dv_z/dt is obtained under space focusing as described earlier [Eq. (1)]. Under nonspace focusing conditions, dv_z/dt is a complicated function. The κ term encompasses a set of constants that includes laser intensity, molecular beam density, ionization efficiency, detection sensitivity, etc.

The differential cross section for single-photon photodissociation with respect to fragment speed v and recoil solid angle Ω is given by

$$\frac{d^2\sigma}{d\Omega\ dv} = \frac{\sigma}{4\pi}[1+\beta(v)P_2(\cos\theta)]P(v) = \frac{\sigma}{4\pi}[1+\beta(v)P_2(\cos\alpha)P_2(\cos\theta_z)]P(v). \tag{6}$$

It is convenient to express the differential cross section in terms of a velocity-dependent angular distribution and an angle-averaged speed distribution $P(v)$. A velocity-dependent anisotropy parameter $\beta(v)$ may arise in collisionless photodissociation for nonimpulsive dissociation where a range of dissociation lifetimes can lead to a time-dependent velocity distribution. It can also occur for competing dissociation pathways that give products with different β values (e.g., the O_3 results in Sec. VI). A velocity-dependent anisotropy is also expected for collisional processes, such as photodissociation in van der Waals complexes. The separation of the angular and velocity parts is not necessary for the following analysis, but is done for convenience. In the second line of Eq. (6), we have transformed to the laboratory drift tube z axis where $d\Omega = \sin\theta_z\, d\theta_z\, d\varphi_z = 2\pi \sin\theta_z\, d\theta_z$ is the laboratory-frame solid angle. The angle θ is the recoil angle relative to the electric field axis ϵ_d and α is the angle of ϵ_d relative to the z axis. Hence the photofragment recoil angle relative to the z axis is $\theta_z = \theta + \alpha$. The second Legendre polynomial is defined as $P_2(x) = (3x^2-1)/2$ and β is the anisotropy factor for the angular distribution. The maximum anisotropies for parallel and perpendicular transitions are 2 and -1, respectively, and a value of 0 corresponds to an isotropic angular distribution.

We denote the observed TOF spectrum $I(t)$ in velocity units $I(v_z)$ for convenience. Because of the linear relationship between t and v_z for space-focusing conditions [see dv_z/dt term in Eq. (5)], the Jacobian transform $I(v_z) = I(t)dv_z/dt$ is a constant. This is not the case for photofragment translational energy spectroscopy where v and t are inversely proportional, in which case a Jacobian must be applied in transforming from t to v. In the present case, a Jacobian appears in the relation between $I(v_z)$ and the c.m. velocity distribution $P(v)$ as shown below. The observed TOF spectrum $I(v_z)$ is obtained by integrating over the area of the detection aperture. Ideally, the detection efficiency $\eta(v_r)$ as a function of the radial velocity v_r, is described by a step function. However, the ion packet that is imaged onto the detection aperture can potentially have some blurring due to field distortions at the grids in the acceleration region (see Sec. VII A). In this general case, the TOF spectrum is described by

$$I(v_z) = \int_0^\infty \frac{d^2N}{dt\ dv_r'}\,\eta(v_r')dv_r' = \kappa\int_0^\infty \frac{1}{v^2}\frac{d^2\sigma}{d\Omega\ dv}\,\eta(v_r')v_r'\ dv_r'. \tag{7}$$

If we assume a step function detection efficiency such that $\eta(v_r)=1$ or 0 for v_r, respectively, less than or greater than the aperture radius δ_r (in velocity units, Sec. II B), then Eq. (7) simplifies to

$$I(v_z) = \kappa\int_0^{\delta_r} \frac{1}{v^2}\frac{d^2\sigma}{d\Omega\ dv}\,v_r'\ dv_r'. \tag{8}$$

It is sometimes convenient to integrate over v by the change of variables $v_r\ dv_r = v\ dv$ to give

$$I(v_z) = \kappa\int_{v_{\min}}^{v_{\max}} \frac{1}{v}\frac{d^2\sigma}{d\Omega\ dv}\,dv \tag{9}$$

where $v_{\min} = v_z$ and $v_{\max} = (v_z^2+\delta_r^2)^{1/2}$. These limits represent the range of v values that can project to a specific value of v_z.

B. Core sampling

For core sampling conditions, where $\delta_r \ll v$ one has the relation $v_z \approx v$. If the velocity distribution is slowly varying over dv, then Eq. (9) simplifies to

$$I_\alpha(v_z) = \kappa\frac{\delta_r^2}{2v_z^2}\left[\frac{d^2\sigma}{d\Omega\ dv}\right]_\alpha. \tag{10}$$

The product $v_z^2 I_\alpha(v_z)$ is directly proportional to the differential cross section for the molecular scattering angle $\theta=\alpha$. When $\delta_r \ll v$ is not satisfied, such as when v is small, v_z ceases to be a good measure of v. Then the integral in Eq. (8) or (9) must be carried out explicitly and determinations of differential cross sections from $I(v_z)$ measurements must be obtained by a fitting or inversion routine (e.g., the appendix).

Calculated TOF spectra for various cases of v and δ_r, ranging from core sampling to 1D projections are presented in Fig. 4. For $v/\delta_r \leqslant 1$, a pure 1D projection is observed. Interestingly, v/δ_r does not have to be very large to give an accurate measurement of $P(v)$ by core sampling. The case for $v/\delta_r = 4$ in Fig. 4 corresponds to a $\Delta v/v$ of 0.03 [Eq. (4)].

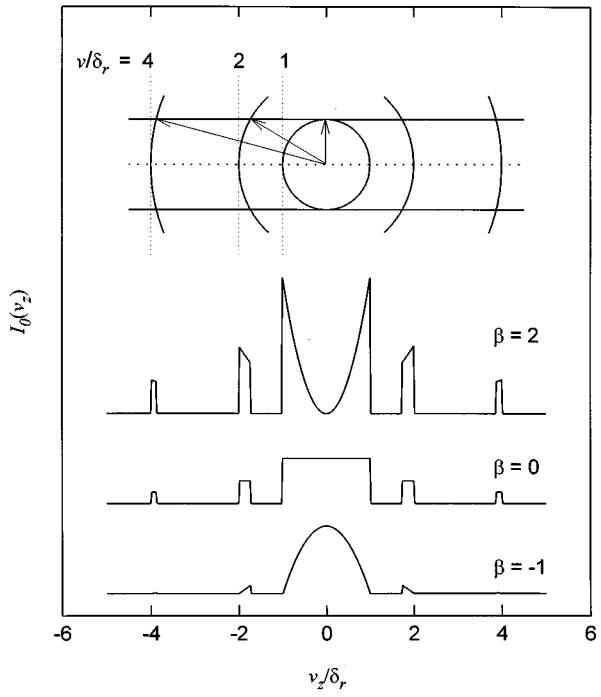

FIG. 4. Calculated TOF spectra for delta function velocity distributions as a function of radial resolution δ_r.

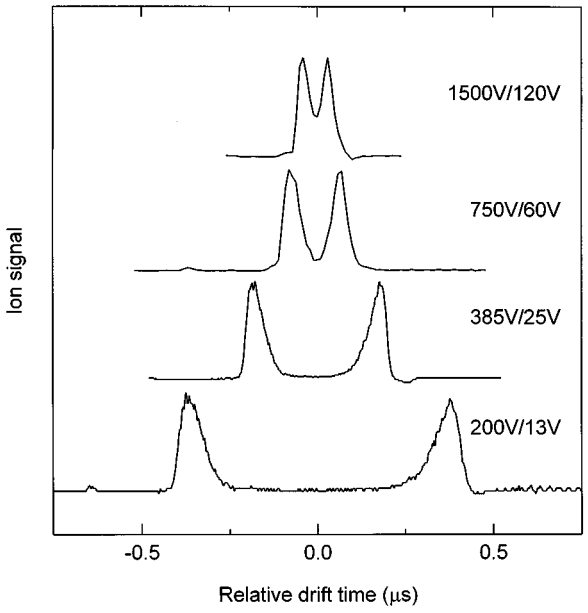

FIG. 5. Observed 1D TOF spectra as a function of acceleration voltages. The sequence of spectra show the transition from 1D projection to core sampling conditions. All spectra were recorded under space focussing condition.

Because δ_r is inversely proportional to the drift time t_0, core sampling conditions are obtained experimentally by choosing suitable extraction and repeller voltages. The effect of increasing t_0 by decreasing the acceleration of the ions into the drift tube is presented in Fig. 5 for detection of I atom in CH_3I photodissociation.

C. Photofragment imaging

2D sectional images are obtained from a series of 1D core TOF spectra, each of which is displaced from the symmetry axis centerline by radial velocity v_r [equal to v_x or v_y depending on plane of detection due to relation $v_r=(v_x^2+v_y^2)^{1/2}$]. The expressions that we have thus far derived for $I_\alpha(v_z)$ are for TOF measurements through the center of the 3D velocity distribution, corresponding to a nominal value of $v_r=0$. Eq. (8) may be generalized to arbitrary v_r offsets by redefining the integration limits as $v_r-\delta_r$ and $v_r+\delta_r$. It follows that $I_{vr}(v_z)$ is given by

$$I_{v_r}(v_z)=\frac{\delta_r}{4v_r}\,\kappa\int_{v_r-\delta_r}^{v_r+\delta_r}\frac{1}{v^2}\,\frac{d^2\sigma}{d\Omega\;dv}\,v_r'\;\;dv_r', \tag{11}$$

where the leading term is the ratio of the area of the detection aperture to that of the annulus defined by the integration limits. In the core sampling limit, Eq. (11) reduces to

$$I_{v_r}(v_z)=\kappa\,\frac{\delta_r^2}{2(v_z^2+v_r^2)}\left[\frac{d^2\sigma}{d\Omega\;dv}\right]_{v_r}, \tag{12}$$

which is the generalized form of Eq. (10) for TOF spectra displaced along the radial coordinate (either x or y). The set of 1D core TOF spectra forms a 2D Cartesian flux map denoted as $P(v_z,v_r)$ and defined as

$$P(v_z,v_r)=\cup_{v_r}\{I_{v_r}(v_z)\}\propto\frac{1}{(v_z^2+v_r^2)}\,\frac{d^2\sigma}{d\Omega\;dv} \tag{13}$$

where $\cup_{v_r}$ denotes the union or set of TOF spectra for increments of v_r. $P(v_z,v_r)$ is directly related to the differential cross section weighted by velocity according to Eq. (13). The integrity of Eq. (13) depends on the v_z and v_r instrument resolutions. An illustration is given in Fig. 6. In Fig. 6(a) are calculated $I_{vr}(v_z)$ plots by Eq. (13) using the $P(v)$ distribution measured previously for $I(^2P_{3/2})$.[32,33] These plots are convolved with the known instrument temporal and radial resolution functions in Fig. 6(b). The measured 2D sectional image is given in Fig. 6(c) and compares well to the calculated image in Fig. 6(b). The instrument functions were necessary in the analysis of Fig. 6 because of the low velocity of the I atom. The detection of a heavy mass in a heavy–light photodissociation represents a challenging application.

The fidelity of Eq. (10) and (13) depends on how well core sampling conditions are satisfied. This condition breaks down as $v\to 0$. Another way to view this is that the angular resolution deteriorates in this limit, a condition that affects virtually all techniques that measure velocity distributions. If an accurate determination of the low velocity part of a distribution is needed, then a fitting routine is required. Fitting algorithms are described in the appendix.

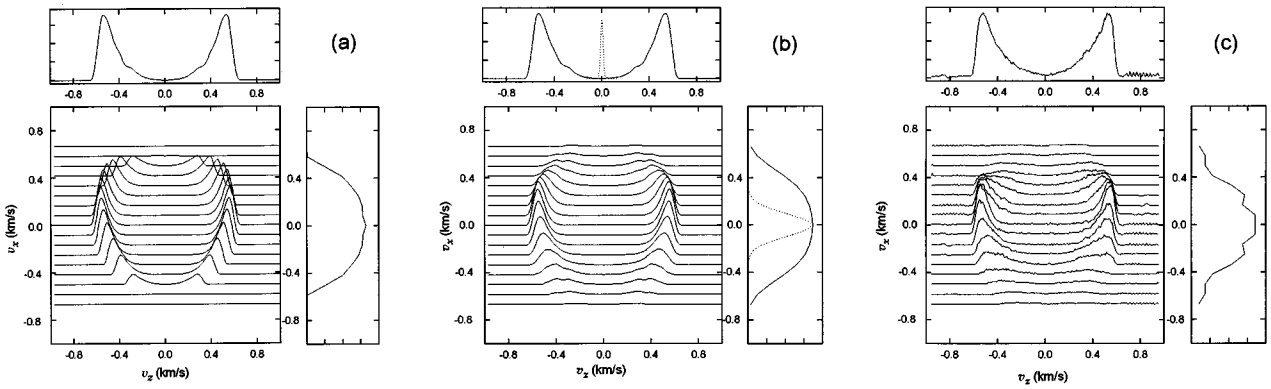

FIG. 6. Comparison of calculated and observed 2D Cartesian maps $P(v_z,v_x)$ of $I(^2P_{3/2})$ from CH_3I photodissociation at 266 nm. 1D projections were obtained by summing $P(v_z,v_x)$ over the appropriate axis. (a) Calculated using previously reported $P(v)$ and β. (b) Calculated map convolved with instrument functions shown on 1D plots. (c) Observed image. The dotted lines on the 1D plots in (b) are the instrument velocity resolutions.

D. Differential cross sections

In the following we summarize some important relations and introduce terminology familiar to bimolecular reactive scattering experiments.

1. Solid-angle differential cross sections

$$\frac{d^2\sigma}{d\Omega\, dv} \propto P(\theta,v)=(v_z^2+v_r^2)P(v_z,v_r), \tag{14}$$

$$\frac{d^2\sigma}{d\Omega\, dE_t}=\frac{d^2\sigma}{d\Omega\, dv}\left|\frac{dv}{dE_t}\right| \propto \frac{P(\theta,v)}{v}$$
$$=(v_z^2+v_r^2)^{1/2}P(v_z,v_r), \tag{15}$$

where $E_t=mv^2/2$ is fragment kinetic energy. $P(\theta,v)$ is defined as the molecular c.m. flux-velocity distribution and represents the ion flux distribution for a constant solid angle of detection in the c.m. frame. The Cartesian flux distribution $P(v_z,v_r)$ is based on a solid angle of detection that is constant in the laboratory frame and, therefore, is a (simple) function of fragment velocity. Based on the above derivations and visualization in Fig. 3, the conversion is simply v^{-2}. Because the laboratory and molecular frames share the same c.m. origin and the observed 2D sectional images measure $P(v_z,v_r)$, rather than projections, no transformations are needed to determine the differential cross sections, as long as core-sampling conditions are valid.

2. Angle-averaged velocity and translational energy distributions

$$\frac{d\sigma}{dv}=\int \frac{d^2\sigma}{d\Omega\, dv}\, d\Omega \propto \int\int P(\theta,v)\sin\theta\, d\theta\, d\varphi$$
$$=P(v), \tag{16}$$

$$\frac{d\sigma}{dE_t}=\frac{d\sigma}{dv}\left|\frac{dv}{dE_t}\right| \propto \frac{P(v)}{v} \propto P(E_t). \tag{17}$$

The above procedure is required when the angular distribution cannot be described by a simple expression such as Eq. (6). Such would be the case for bimolecular reactive scattering, and photodissociation in van der Waals complexes. Equation (6) is generally a sufficient description of one-photon dissociation in isolated molecules, in which case $P(v)$ can be determined from selected 1D TOF spectra under core sampling conditions. Some useful methods that follow from Eqs. (6) and (10) are

$$P(v)\propto v_z^2 I_{54.7}(v_z), \tag{18a}$$

$$P(v)\propto v_z^2[I_0(v_z)+2I_{90}(v_z)], \tag{18b}$$

$$P(v)\propto \frac{v_z^2 I_0(v_z)}{1+\beta(v_z)}. \tag{18c}$$

Equation (18a) corresponds to detection of product at the magic angle relative to the laser polarization axis. $P(v)$ is directly measured because the velocity and angular distributions decouple at the magic angle. Because the angular distribution is usually of interest, it is useful to record 1D TOF spectra at the recoil angles 0 and 90° to determine $P(v)$ and $\beta(v)$. $P(v)$ is expressed by Eqs. (18b) and (18c) and $\beta(v)$ is given by

$$\beta(v)=\frac{I_0(v_z)-I_{90}(v_z)}{\frac{1}{2}\, I_0(v_z)+I_{90}(v_z)}. \tag{19}$$

Equation (19) can be derived from Eqs. (6) and (10) under core-sampling conditions.

If anisotropy is independent of velocity [e.g., $\beta(v)=\beta$], then a single TOF spectrum $I_0(v_z)$ is sufficient to determine $P(v)$ according to Eq. (18c). For an isotropic Maxwell–Boltzmann distribution, $P(v)\propto I_0(v_z)/v_z^2$ regardless of whether core-sampling conditions hold (see the appendix). In all cases above $P(E_t)\propto P(v)/v$ [Eq. (17)]. Finally, the c.m. translational energy is computed from

$$E_{t,\text{c.m.}}=E_t\left(\frac{M}{M-m}\right), \tag{20}$$

where m is the detected fragment mass and M is the molecular precursor mass.

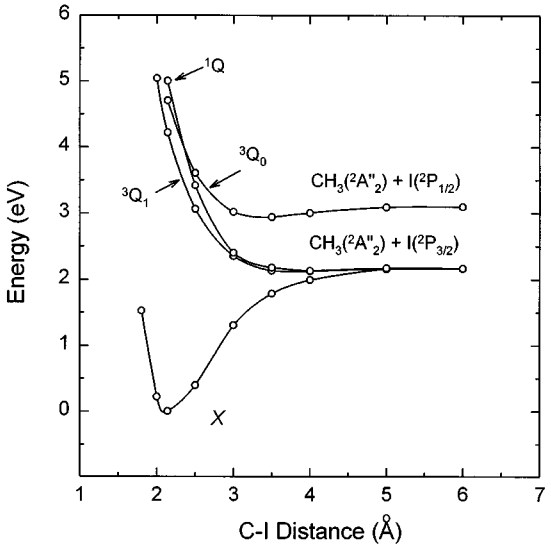

FIG. 7. Potential energy curves for the ground electronic state X and the optically active dissociative A states. Symbols are calculated values from Tadjeddine *et al.* (Ref. 36).

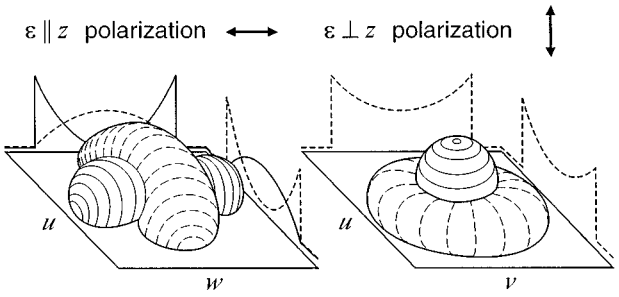

FIG. 8. Representation of the photofragment angular probability distribution for parallel and perpendicular transitions of CH_3I. The image planes uw and uv cut through different sections of the angular probabilities. The uv plane, by lying in the node of the parallel distribution, discriminates effectively against parallel photofragment recoil, thereby enabling sensitive detection of fragment recoil from perpendicular transitions. The detection plane is varied by rotating the laser polarization axis. The calculated curves along the edges are the 1D projections of the 2D intensity profile for a delta function velocity distribution.

V. PERPENDICULAR $A \leftarrow X$ TRANSITIONS IN CH_3I

In this section we present new results on the angle-velocity distributions for photofragments $I(^2P_{3/2})$ and $I(^2P_{1/2})$ (henceforth I and I*) resulting from the A-state photodissociation of CH_3I at 266 and 304 nm. Preliminary results have been presented before.[28] The intent here is to also focus on the instrumental conditions and constraints to recording photofragment images by the present technique.

A. Background

A potential energy curve for the optically active $A \leftarrow X$ transitions is plotted along the C–I coordinate in Fig. 7. In the Franck–Condon region, the order of these states by increasing energy is $^3Q_1$, $^3Q_0$, and ^1Q (or $2E$, $2A$, and $3E$ in C_{3v} Mulliken notation).[34] These transitions are due to $5pn \rightarrow \sigma^*$, of which there are a total of five final electronic states (two are electric-dipole forbidden from X). The $^3Q_0$ state is reached by a transition moment parallel to the C–I principal and bond-breaking axis, and the $^3Q_1$ and ^1Q state are reached by a perpendicular transition moment. The parallel transition correlates to the CH_3+I dissociative limit and the perpendicular transitions to the CH_3+I^* limit.[34–37] A surface crossing is evident in Fig. 7 along the $^3Q_0$ and ^1Q potential curves.

Based on the excited-state correlations in the diabatic picture of the A states (i.e., allowed crossings), one would expect angular distributions for the I and I* fragments that peak perpendicular ($\beta=-1$) and parallel ($\beta=2$), respectively, to the laser polarization axis. Instead, previous anisotropy measurements show that I and I* both display parallel-like dissociations.[16,32,33,38–40] This observation can be explained by a strong $^3Q_0$ transition that branches at the surface crossing to give both I and I* product. Potential energy calculations indicate that the surface crossing is avoided, thus supporting the experimental findings.[35–37] In measurements of A state emission, Butler and co-workers observed that the emission polarization evolved from a pure parallel component to a mixture of parallel and perpendicular components, supporting the surface branching picture.[41]

The questions we attempt to answer here are: (1) what are the cross sections for direct excitation of the apparently weak perpendicular states, (2) what is the crossing probability between the $^3Q_0 - ^1Q$ surfaces, (3) what is the I/I* branching ratio, and (4) how do these properties vary with excitation wavelength, and (5) how well are these properties predicted by the latest calculations of the potential energy surfaces?

B. Results

To directly probe photofragmention that occurs specifically from either parallel or perpendicular transitions requires a technique that specifically detects photofragments that recoil parallel vs perpendicular to the excitation polarization axis ϵ_d. The method of detecting sectional 2D photofragment images offers this capability. The principal challenge is to detect the weak perpendicular photofragment yield while discriminating against the strong parallel component.

Two photofragment planes of detection are needed to selectively detect perpendicular and parallel photodissociation. In the body-fixed polarization frame in Table I and Fig. 3, one finds that uv plane probes dissociation perpendicular to ϵ_d and the uw (also vw) plane probes parallel to ϵ_d. These two planes correspond to the laboratory xz plane where the laser polarization is aligned either perpendicular or parallel to the drift tube axis z, respectively (cf. Table I and Figs. 2 and 3). The diagram in Fig. 8 illustrates the angular distributions of product that are detected by the uw and uv planes. The uw plane detects both parallel and perpendicular product recoil, but is optimized for the former. The uv plane, however, selectively detects just perpendicular product recoil. The importance of a sectional image in this case is that it offers high discrimination against detecting parallel recoil by

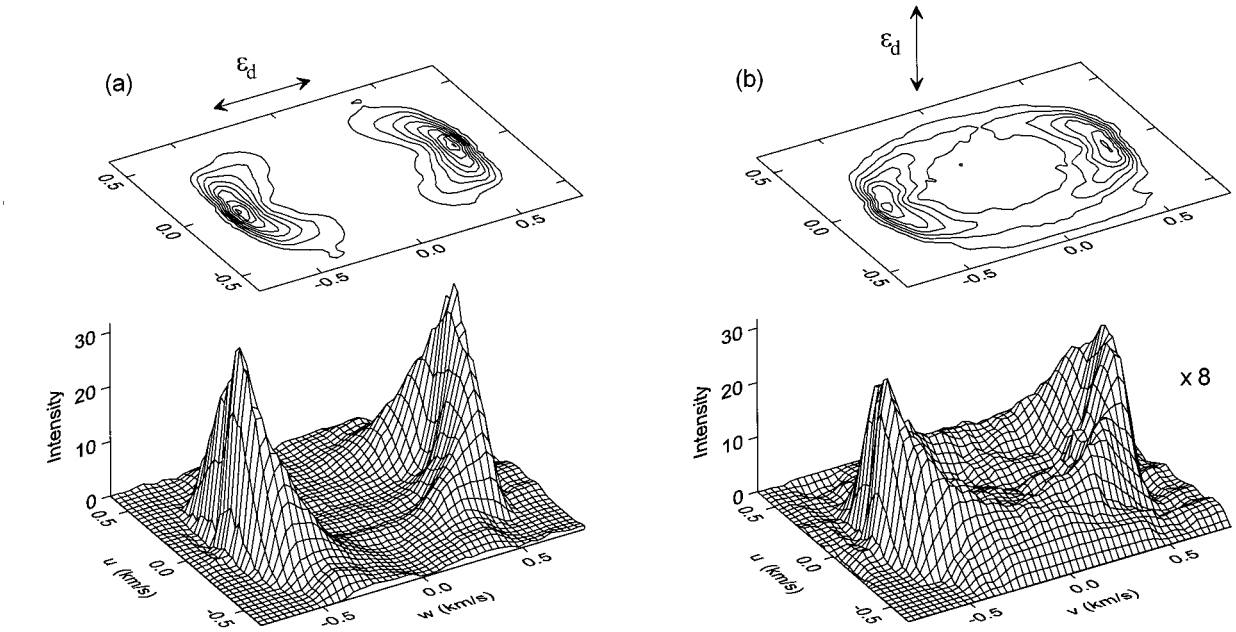

FIG. 9. 2D sectional image of $I(^2P_{3/2})$ from CH_3I photodissociation at 266 nm presented as surface and contour plots. (a) $\epsilon_d \| z$, (b) $\epsilon_d \perp z$. The velocity planes are represented in the body-fixed coordinate system.

virtue of lying in the node of the parallel angular distribution. The extent of discrimination depends on how thin the planar section is, an issue that we address shortly.

Photodissociation was measured at 266 and 304 nm, which is at the peak and the red edge of the *A* band, respectively. Excitation of I and I* is achieved by 2+1 resonance-enhanced multiphoton ionization (REMPI) at 304.7 nm ($6P^2D^0_{5/2}$ intermediate state) and 304.0 nm ($6P^4D^0_{1/2}$ state), respectively.[42] Because we are concerned with detecting direct excitation of the perpendicular transitions, which correlate with I, we present images for the $I(^2P_{3/2})$ fragment only. Photofragment images in the *uw* and *uv* planes are presented in Figs. 9–11 for 266 and 304 nm photolysis. A strong forward–backward peaked angular distribution is observed for the *uw* plane, corresponding to product that recoils parallel to ϵ_d due to the strong parallel transition to the $^3Q_0$

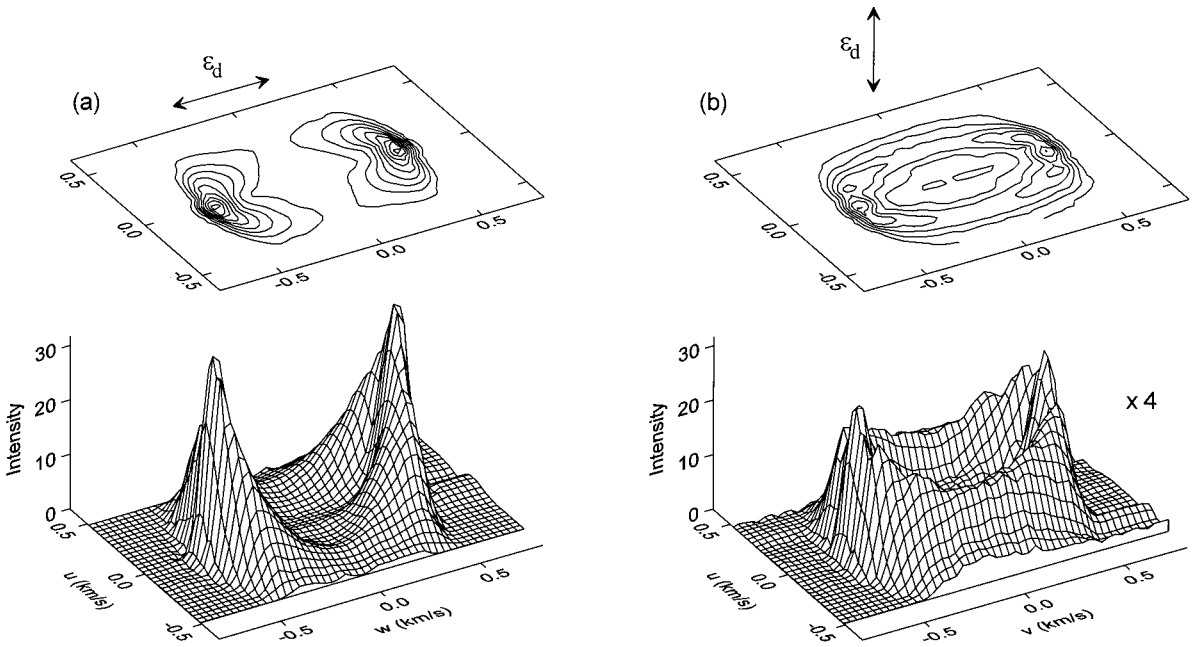

FIG. 10. Same as Fig. 9, except 304 nm photodissociation.

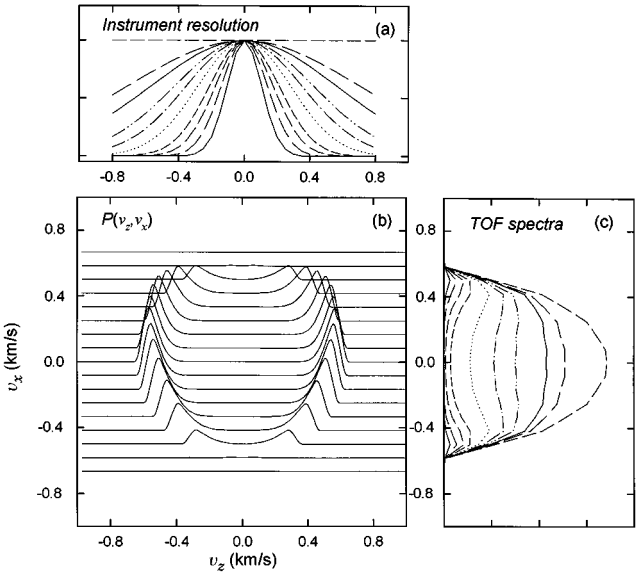

FIG. 11. The effect of radial instrument resolution on TOF spectra for perpendicular detection $\epsilon_d \perp z$ in the presence of strong parallel product recoil. (a) Varying Gaussian radial resolution functions. (b) Assumed angle-velocity distribution [see Fig. 6(a)]. (c) Calculated TOF spectrum $I_{90}(v_z)$ resulting from acceptance of high recoil-angle photofragments from parallel excitation.

state. As mentioned above, perpendicular product recoil will also appear in this plane perpendicular to the parallel axis. There is some evidence of perpendicular product recoil in the uw image for 304 nm excitation; however, the signal is weak and not very convincing because of the presence of a strong parallel signal. However, in the uv image plane, which lies in the node of the parallel distribution, the I atom signal due to perpendicular recoil, though weak, is in clear evidence in Figs. 9 and 11. The characteristic ''donut'' shaped image in the uv plane occurs because the angular distribution peaks at an angle $\theta=90°$ relative to ϵ_d, but is invariant about the azimuthal angle about ϵ_d.

C. Instrument effects

The maximum I atom velocity is about 0.8 km/s, which corresponds to a Doppler shift along the laser propagation x direction of about ± 0.09 cm^{-1}. The bandwidth of the laser used to record the images in the xz laboratory planes is $\geqslant 0.30$ cm^{-1} indicating that all ions are ionized with nearly equal probability in the 2D images. Were this not the case, then only the yz laboratory frame would give undistorted 2D sections. In Sec. VI, we present images in the yz plane for O atom from O_3 photodissociation, where the fragment velocities, and hence, Doppler shifts are about an order of magnitude greater than for I atom from CH_3I photodissociation. The ion TOF method is much better suited than Doppler spectroscopy for slow velocity fragments. The v_z resolution of about 0.03 km/s obtained here for I atom corresponds to a Doppler shift resolution of about 0.003 cm^{-1}.

We now turn our attention to the instrument factors that can limit angle-velocity resolution and how they affect the observed planar images. For instance, the uv image, which purports to discriminate against parallel recoil, can be contaminated from parallel excitation by product that recoils at large angles. The extent of discrimination depends on how thin the planar section is, which in turn depends on the detection aperture size and other instrument broadening effects. In fact such contamination is present in the uv images in Figs. 9 and 10. Rather than observing a purely symmetric ''donut-shape'' distribution due to perpendicular product recoil, a forward–backward v-velocity component appears superimposed along the $u=0$ centerline. This is due to ''leakage'' of high angle product recoil from the strong $^3Q_0$ parallel transition. The predicted signal as a function of an instrument resolution function is presented in Fig. 11. The instrument resolution in Fig. 11(a) is represented by a Gaussian function of varying width and includes broadening due to aperture size, blurring of the image by the ion optics, and slight misalignment of the laser polarization axis from pure $\alpha=0°$ and 90° relative to the drift tube z axis. The calculated angle-velocity distribution from parallel transition [from Fig. 6(a)] is given in Fig. 11(b). The resultant TOF spectrum that would appear in the perpendicular image (e.g., along the $u=0$ centerline in Figs. 9 and 10) is given in Fig. 11(c). The results observed here are consistent with an instrument resolution represented by a Gaussian width of 0.15 km/s, and corresponds to an angular resolution for the centerline 1D TOF spectrum of $\pm 7\%$ for the highest velocity fragments. (The estimated instrument broadening is consistent with a series of 1D TOF spectra recorded for recoil angles $\theta=0°$ and 90° and is also consistent with the results in Fig. 6.) The detector aperture diameter is 5 mm. Based on an I atom drift time of 72 μs in these experiments, the above analysis indicates an effective aperture resolution of about 10 mm. Other instrument tests are in agreement with this analysis. Some improvement in resolution has been made subsequent to this work, and further potential improvements are enumerated in Sec. VII.

The kinematics of a particular photodissociation can have a large bearing on the measured angle-velocity resolution. Detection of very slow fragments such as when monitoring a heavy fragment in a heavy–light dissociation are difficult for almost any technique that measures translational energy. The present method is favored by fragments that carry high recoil velocity as this leads to greater spreading of the ion packet upon reaching the detector. In this regard the detection of I atom in the photodissociation of CH_3I represents a very unfavorable case. It follows from Eq. (21) that the I atom velocity is given by $v_I^2=(E_t/m_I)(m_{CH_3}/m_{CH_3I})$. The I atom fragment has a very low velocity because of its heavy mass and because it recoils off a light mass.

D. Anisotropies, relative cross sections, branching ratios, and surface-crossing probabilities

2D sectional images are useful for visualizing angle-velocity distributions and for searching for properties that deviate from the second moment of the Legendre polynomial dependence described by Eq. (5). However, for simple

TABLE II. Measurements of anisotropy, relative cross sections, spin–orbit branching ratios, and surface crossing probabilities as a function of excitation wavelength.

λ (nm)	β_I	β_{I^*}	$\sigma_\perp/\sigma_\parallel$	f_I/f_{I^*}	p
266	1.8±0.1	1.9±0.1	0.05±0.04	0.37[a]	0.25±0.05
304	1.5±0.1	1.9±0.1	0.20±0.05	1.1±0.2	0.43±0.08

[a]References 44 and 45.

single-photon photodissociation, the anisotropy β and velocity distribution $P(v)$ can be measured from 1D core sampling TOF spectra recorded at recoil angles $\theta=0°$ and 90° as outlined in Sec. IV D. In this regard, we have augmented our 2D images data set with high resolution measurements of $I_0(v_z)$ and $I_{90}(v_z)$. Similarly, it can be shown that the ratio of cross sections for perpendicular and parallel transitions is given by $\sigma_\perp/\sigma_\parallel=2I_{90}/I_0$. A data set of $I_0(v_z)$ and $I_{90}(v_z)$ traces have been recorded for 266 and 304 nm pump excitation and I and I* probe detection.

Measured values of β and $\sigma_\perp/\sigma_\parallel$ are compiled in Table II. Gedanken and Rowe recorded absorption and magnetic circular dichroism (MCD) spectra of CH_3I, from which they determined the $^3Q_1$, $^3Q_0$, and ^1Q component contributions to the A absorption band.[43] The peak component absorption wavelengths (and percentage total absorption strengths) reported are 300 (1%), 261 (78%), and 240 nm (21%), respectively. The MCD results show a minimum in $\sigma_\perp/\sigma_\parallel$ at 260 nm, which is consistent with our results. The A band intensity is down considerably at 304 nm relative to its peak. Hence it is difficult to estimate the $\sigma_\perp/\sigma_\parallel$ ratio for the $^3Q_1$ and $^3Q_0$ transitions at this wavelength from the MCD spectra. However, based on the peak wavelengths for these components, one expects a ratio $\sigma_\perp/\sigma_\parallel$ that is greater at 304 nm than at 266 nm, in accord with the results in Table II. These results also conform with calculations of the A state potential energy surfaces.[35]

The different β values measured for I and I* are attributed to different admixtures of parallel and perpendicular absorption components. Anisotropy is also dependent on photodissociation lifetime. However, we believe this is unlikely to explain the measurements here because (1) this would require that I and I* have different formation lifetimes, which is unexpected, and (2) considering that lifetime does not significantly reduce anisotropy in studies using effusive (warm) CH_3I expansions,[32,33,39] it is unlikely that for supersonic expansions that the rate of molecular rotation would compete with photodissociation. Therefore, we conclude that the β value is due primarily to the ratio $\sigma_\perp/\sigma_\parallel$.

An important measurement in this work is the surface crossing probability p due to the $^1Q-{}^3Q_0$ intersection. The property can be determined from measurements of $\sigma_\perp/\sigma_\parallel$ and the branching ratio f_I/f_{I^*}. If we assume that the lower energy surface $^3Q_1$ does not participate in a crossing with $^3Q_0$ in the Franck–Condon region of excitation and dissociation (as predicted in Fig. 7), then the relative yield of I and I* can be expressed by

$$f_I=(1-p)\sigma_\perp(^1Q)+p\sigma_\parallel(^3Q_0)+\sigma_\perp(^3Q_1), \tag{21a}$$

$$f_{I^*}=p\sigma_\perp(^1Q)+(1-p)\sigma_\parallel(^3Q_0). \tag{21b}$$

Our experiment currently does not distinguish $\sigma_\perp(^1Q)$ and $\sigma_\perp(^3Q_1)$; however, because these transitions are well separated in energy,[35,43] we can make the reasonable assumption that $\sigma_\perp(^1Q)\gg\sigma_\perp(^3Q_1)$ at 266 nm and $\sigma_\perp(^1Q)\ll\sigma_\perp(^3Q_1)$ at 304 nm. This renders Eqs. (21) solvable. The branching ratio f_I/f_{I^*} is measurable from the ratio of ion signal for I and I*. To calibrate the detection efficiency, we use ratios at 266 nm measured previously of $f_I/f_{I^*}=0.37$.[44,45] The change in ratio of the measured ion signal for I and I* at 304 vs 266 nm provides the information needed to obtain the value $f_I/f_{I^*}=1.1$ at 304 nm.[30] A photoacoustic measurement gave a value of about 2.0.[46] The resultant surface crossing probabilities are reported in Table II.

The ability to calculate interactions between potential energy surfaces is an important test of computational theory. Shapiro calculated $^1Q-{}^3Q_0$ crossing probabilities of about 0.32 and 0.50 for 266 and 304 nm excitation, respectively.[35] These results are in reasonable agreement with the measured values in Table II. It is important to note that both the measured and calculated p values increase with decreasing excitation energy. This trend may be explained by a Landau–Zener type argument wherein the surface crossing probability or adiabaticity of staying on the lower surface increases with decreasing velocity through the crossing region.

VI. HARTLEY BAND EXCITATION: $O_3\rightarrow O(^3P_j)+O_2(X,v)$

In a previous study we reported on the photofragment angle-velocity distributions of the $O(^3P_{j=0,1,2})$ states for ozone photolysis at 226 nm by 2+1 REMPI in a time-of-flight mass spectrometer (TOFMS).[29] Photofragment images and 1D TOF spectra were recorded from which velocity dependent anisotropy $\beta(v)$ and translational energy distributions were measured. This work was compared to similar measurements by Miller *et al.*,[47] which included photofragment images by the Houston group. The objective of these studies was to test for a possible newly identified source of O_3 production in the upper stratosphere. The O atom photofragment images lead to fragment translation energy distributions, which in turn enable a determination of the O_2 vibrational distributions.

Although, we present additional data from our earlier report,[29] our primary objective here is to discuss instrumental conditions and operational constraints in recording photofragment images as sections.

A. Background

Wodtke and co-workers[47–49] recently proposed, based on experimental evidence, a source of O_3 production involving the reaction of highly vibrationally excited O_2 with ambient O_2 as follows

$$O_2(v\geqslant 26)+O_2\rightarrow O_3+O. \tag{22}$$

This reaction is of current interest because it could possible explain a discrepancy that is believed to exist between calculated and observed ozone levels in the upper

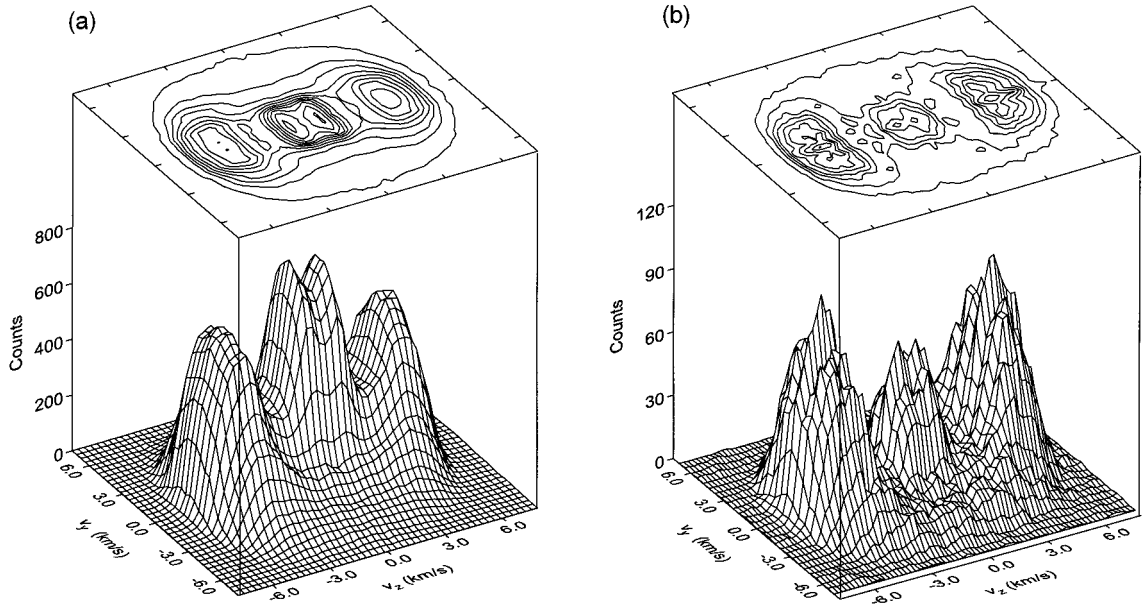

FIG. 12. 2D photofragment image for $O(^3P_j)$ angle-velocity distribution at 226 nm. The laser polarization vector is aligned with the drift-tube axis ($\epsilon_d \| z$). Results are presented for the (a) $j=2$ and (b) $j=1$ spin–orbit states. Intensity scales in (a) and (b) are unrelated.

stratosphere.[50] The importance of reaction (22) toward explaining the ozone discrepancy problem depends on the yield of $O_2(v \geqslant 26)$ formed by photolysis of ozone. Ozone photolysis occurs primarily by singlet state absorption and leads to the spin-allowed dissociation channels

$$O_3 + h\nu \rightarrow O_2(a\ ^1\Delta_g) + O(^1D) \tag{23}$$

$$\rightarrow O_2(X\ ^3\Sigma_g) + O(^3P). \tag{24}$$

The branching ratio of $O(^1D)/O(^3P)$ is about 0.90/0.10 for wavelengths short of 310 nm.[51] The level of vibrational excitation needed for reaction (22) to occur can only result by ground electronic state $O(^3P)$ production and has a photochemical threshold for production of 243 nm. The Houston and Wodtke groups used photofragment imaging to measure the $O(^3P_j)$ translational energy spectrum and observed a bimodal distribution for 226 nm photolysis, corresponding to $O_2(v)$ distributions peaking at $v=14$ and $v=27$.[47] Our photofragment imaging work, published elsewhere[29] and here support these results.

There have been several previous reports of ozone photodissociation studies by some form of photofragment translational energy spectroscopy or Doppler spectroscopy.[52–56] Whereas there is reasonable consistency in the reported fragment velocity distributions, the measured anisotropies show significant variations, only part of which can be attributed to different excitation conditions.

B. Results

In the results presented here, the pump and probe excitation are from the same 5 ns laser pulse at 226 nm. $O(^3P_{0,1,2})$ were ionized by 2+1 resonance-enhanced multiphoton ionization (REMPI) through the two-photon transition $3p\ ^3P_{0,1,2} \leftarrow 2p\ ^3P_{0,1,2}$. 2D sections of the 3D velocity distributions are presented in Fig. 12 for the fragment $O(^3P_j)$ for $j=2$ and 1. The ϵ_d vector is aligned along the drift-tube z axis. The laboratory plane of detection is yz, which is obtained by scanning the y-deflector plates (Table I). Because of axial symmetry about z, a xz image in principal would give the same result. However, because the Doppler width of the O atom is greater than the laser bandwidth, the plane that is orthogonal to the laser direction of propagation is much preferred. Doppler selection enhances the planarity of the yz image. In contrast, because the xz plane lies along the laser propagation axis, the laser frequency would have to be scanned over the Doppler width to record an undistorted photofragment image (or optimized to the Doppler shift for the particular 1D TOF spectrum in the overall image).

There are three clear observables in the images in Fig. 12: (1) a bimodal velocity distribution is evident, (2) the bimodal distributions are highly peaked and anisotropic, and (3) the relative intensity of the lower-velocity component decreases with j. The higher-velocity signal corresponds to the known $O_3 \rightarrow O(^3P_j) + O_2(X^3\Sigma_g^-)$ dissociation channel. It is formed in a relative yield of about 5:4:2 for $j=2,1,0$, respectively. The high and low-velocity distributions are similar to that observed by Miller *et al.*[47] Results of our work are summarized in Table III. We note that the total yield of $O_2(v \geqslant 26)$ for the $O(^3P)$ channel is 0.08 ± 0.02, which is an increase from our originally reported value.[29] The previous work did not recognize the importance of including $\beta(v)$ in determining $P(v)$, according to Eq. (18c).

One of the purposes of this work was to test the premise by Miller *et al.*[47] that the production of $O_2(v \geqslant 26)$ may explain the ozone deficit problem. In that regard, we have veri-

TABLE III. Branching ratio, vibrational probability, and anisotropy for $O(^3P_j)$ dissociation as a function of spin orbit state j.

			β [a]	
j	f_j	$P(v\geqslant 26)$	high	low
2	0.45±0.1	0.110±0.03	1.1±0.1	0.4±0.2
1	0.36±0.1	0.059±0.02	1.2±0.1	0.5±0.2
0	0.18±0.1	0.046±0.02	1.0±0.1	0.4±0.2

[a]Values are reported for high and low velocity components.

fied the presence of the slow $O(^3P)$ component observed by Miller *et al.* and have measured the relative yield of slow vs fast O atoms. The peak in the vibrational distributions for 226 nm photolysis occurs at $v=15$ and $v=27$, in good agreement with Miller *et al.*

C. Instrumental effects

It was noted earlier that the velocity resolution along the TOF axis z is much better than along the spatial or radial axes x and y. This is borne out by the instrument functions plotted in Fig. 6(b). A combination of the detector aperture diameter and blurring of the ion image due to the deflection by the grid fields currently limits our spatial resolution δ_r to about 0.5 km/s, corresponding to an effective aperture radius of about 8 mm. The time resolution was measured by recording the TOF for thermal O atoms created in the nozzle. This weak signal could be enhanced relative to photodissociated O atoms by synchronizing the laser pulse to the extreme beginning of the gas pulse where the lighter thermal O atoms are enriched relative to O_3. The width of the ion peak was 18 ns, corresponding to a velocity width of about 0.2 km/s.

An important consequence of the limitations on radial velocity resolution is that the core-sampling condition can break down for low velocity fragments. This is the case in Fig. 12, where the low-velocity lobe, which peaks at about 0.9 km/s has significant yield of product with velocities approaching the resolution figure of $\delta_r=0.5$ km/s. This part of the image no longer satisfies the core sampling condition where Eq. (12) holds. To analyze the anisotropy β and velocity distribution $P(v)$ in this region requires fitting the data as described in Appendix A. Attempts to analyze data using the simple core sampling expressions lead to obviously suspect results. An example is given in Fig. 13 for the determination of $\beta(v)$ using Eq. (19) on $I_0(v_z)$ and $I_{90}(v_z)$ 1D TOF spectra. The $\beta(v)$ determination shows a sudden drop to negative values for $v_z<0.8$ km/s. This results because the $I_{90}(v_z)$ signal increases markedly at low v_z. The reason is that the 1D TOF becomes more characteristic of a projection than a core sampling at lower velocities. The effect is illustrated in the calculated spectra in Fig. 4.

D. Differential cross sections

The relationship between the experimentally measured 2D Cartesian velocity map $P(v_z,v_r)$ and the angle-velocity differential cross section is given by Eq. (14). The simple v^2 relationship holds in the core-sampling limit, but breaks down toward the map origin where fragment velocities approach the radial resolution δ_r. A fitting routine described in Appendix A is necessary to model this region accurately required. If angular information is less important than relative intensities, for example when determining $P(v)$, a useful approximation is to modify the v^2 term to reflect the fact that the solid angle of detection reaches a maximum value for $v\leqslant\delta_r$ since all ions are collected (1D projections). One may then approximate Eq. (14) as $P(\theta,v)\propto f(v)P(v_z,v_r)$ where $f(v)=(v+a)^2$. The a term causes the function to role off to a constant value. We used a value of $a=2\delta_r$(1.0 km/s) to calculate the $P(\theta,v)$ map in Fig. 14.

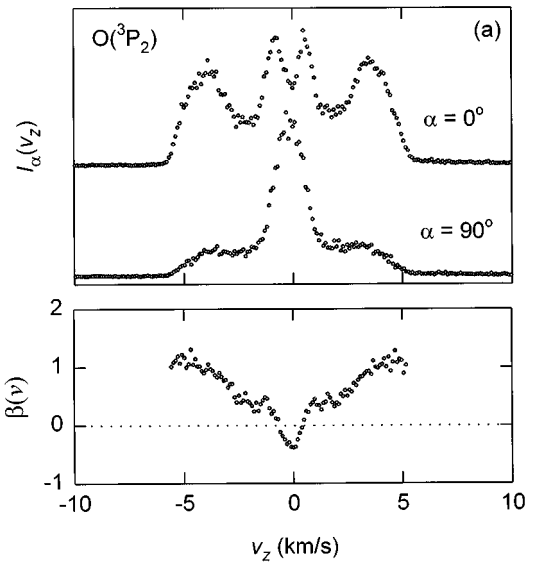

FIG. 13. Angle-resolved $O(^3P_2)$ photofragment velocity distributions $I_\alpha(v_z)$ and velocity dependent anisotropy $\beta(v)$ for O_3 excitation at 226 nm where α is the alignment of ϵ_d relative to z. The figure shows how the validity of using Eq. (19) to determine β breaks down under noncore-sampling conditions. The timescale for the TOF spectra is $t_0=15.1$ μs and $2|t-t_0|=550$ ns for the outer peak onsets.

VII. PROSPECTS AND OUTLOOK

A. Potential performance enhancements

As discussed earlier, the velocity resolution in the spatial dimensions (x,y) is inferior to that in the time dimension (z) because of blurring that results from deflection of ion trajectories at the $V1$ extraction grid (Fig. 2). (The detection aperture was reduced in size until no further improvement in resolution occurred.) The deflection of ion trajectories is due to penetration of the $V0-V1$ field through the $V1$ grid mesh, which creates a periodic field that exerts radial forces on the ions. Bergmann *et al.* formulated the problem of field distortions near wires for the case of parallel wires.[57] For crossed wire mesh, they gave an approximate expression for the change in radial velocity due to field distortions as

$$\Delta v_r=\frac{qE}{2mv_1}\left[y-\frac{a}{2}\right], \tag{25}$$

where q is charge, m is mass, E is the difference in the electric fields on either side of the $V1$ grid, v_1 is the ion

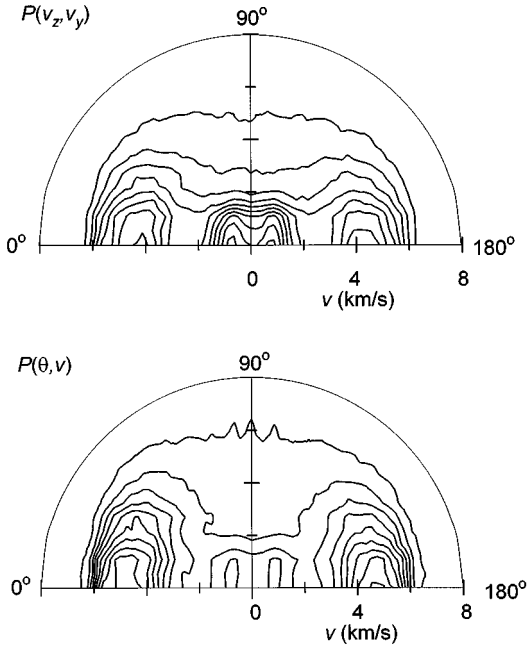

FIG. 14. Hemispheric representation of the experimentally observed cartesian flux map $P(v_z,v_y)$ for $O(^3P_2)$ photofragment from O_3 photodissociation at 226 nm. The solid angle differential cross section represented by the c.m. flux-velocity contour maps $P(\theta,v)$ is obtained by Eq. (14).

velocity at grid $V1$ due to the extraction field, a is the grid spacing, and y is the separation between ion and grid wire at closest approach (the trajectory is assumed to be perpendicular to the grid plane). Using the nomenclature of Wiley and McLaren[31] and assuming an average deflection velocity $\langle \Delta v_r \rangle$ corresponding to $y=a/4$, leads to the expression

$$\langle \Delta v_r \rangle = \frac{aq(E_d - E_s)}{4(2mE_s s_0)^{1/2}} \tag{26}$$

where E_s and E_d are the extraction and acceleration fields between the grid pairs $V2-V1$ and $V1-V0$, respectively, and s_0 is the distance from the ionization volume to the $V1$ grid, which is 0.5 cm. Typical values of E_s and E_d are 15 and 230 V/cm for the CH_3I work and 25 and 400 V/cm for the O_3 work. We currently use electroformed grids having 80 wires/in. and 90% transmission, which corresponds to $a=0.030$ cm. These conditions lead to calculated deflection velocities $\langle \Delta v_r \rangle$ for the CH_3I and O_3 studies of 0.20 km/s for I atom detection and 0.75 km/s for O atom detection. Though these values exceed the respective radial resolutions of 0.015 and 0.50 km/s estimated experimentally, the approximations leading to Eq. (26) are sufficiently good to provide guidance on how to improve the radial resolution. The two most obvious suggestions are: (1) install a finer grid mesh at $V1$ (180 wire/in., 80% transmission are available), and (2) increase the grid spacing between $V0$ and $V1$ (currently 1 cm in our case), in order to decrease the E_d field while maintaining the same final ion energy. These changes should lead to nearly an order of magnitude improvement in the radial resolution.

A natural extension of the imaging technique is to use multichannel TOF detection to replace the process of rastering the ion packet across the detection aperture and recording individual 1D TOF spectra. A possible system would be to use a microchannel plate with a 32-channel segmented anode array to capture the entire width (or halfwidth) of the ion packet. This configuration is similar in concept to the position-sensitive time-of-flight detection reported by Pollard *et al.*,[58] which is a mass-selected 1D projection method that records the spatial distribution of the ions on the detector array to measure $P(v)$. In the present case, data acquisition could be achieved using a commercially available 32-channel 8-hit time-to-amplitude converter (TAC). Such a device would allow a maximum of 256 ion counts per pulse; however half that count rate is a practical limit to maintain valid counting statistics. Bin widths may be varied to as small as a few nanosecond time frame in a total collection time of microseconds. The ability to record single-shot images (with signal averaging to improve signal-to-noise) would improve immunity to instrument temporal variations. Likewise, multiplexed data collection would reduce data collection time proportionately. We estimate that 2D images of the quality reported here could be obtained in a few minutes of signal averaging.

B. Other applications

The 2D imaging by sections method for recording c.m. Cartesian flux-velocity maps was demonstrated for unimolecular photodissociation. However, it is applicable to essentially all manner of scattering, such as due to bimolecular reactive and unreactive collisions, surface scattering, cluster photodissociation, etc. An advantage of recording direct 2D Cartesian images rather than projections is that one can devise ''action-type'' probes whereby an experimental parameter such as wavelength for spectroscopic scans, or time for pump–probe dynamics measurements, can be varied while detecting a fragment or product with state, angle, and velocity specificity. A potential application is to detect quasibound resonances in a dissociative coordinate. If resonances lead to increased lifetimes, then the angular distributions will be markedly changed compared to direct dissociation. Resonances could be detected by recording an excitation spectrum while probing a specific product in a region of θ,v space that is reached primarily by long-lived states (e.g., detecting at 90° for parallel excitations). Such effects may arise from photoexcitation in molecules above a dissociative limit. Similarly, bimolecular scattering resonances may be probed by photodissociation in aligned van der Waals complexes. Resonances may be observed by scanning the photolysis energy as a way to tune the collision energy.[59,60]

Almost all cases of photodissociation and bimolecular scattering are axisymmetric, in which case only one or two 2D images are needed to define the 3D velocity distributions. However, there may be circumstances where an axis of symmetry does not exist (e.g., when stereospecificity, chirality, or surface alignment hold). Then the advantage of recording three orthogonal planar sections becomes indispensible to measuring 3D velocity distributions. The present technique

permits planar sections to be recorded at any angle with any offset in velocity along any axis.

ACKNOWLEDGMENT

This work was funded by the Aerospace Sponsored Research program.

APPENDIX: FITTING ALGORITHMS

Two methods are used to fit data when core sampling conditions are not valid. The first method derives from Eqs. (6) and (7) and involves averaging a series of calculated $I_{vr}(v_z)$ spectra for some trial $P(v)$, weighted by the radial resolution function $\eta(v_r)$. The procedure is described by

$$I(v_z)=\kappa\int_0^\infty \frac{d\sigma}{d\Omega}\frac{P(v)}{v^2}\,\eta(v_r')v_r'\,dv_r'$$

$$=\sum_{v_r} I_{v_r}(v_z)\,\eta(v_r)\Delta v_r$$

$$=\kappa\sum_{v_r}\frac{P_{v_r}(v_z)}{(v_z^2+v_r^2)}\frac{d\sigma}{d\Omega_{v_r}}\,\eta(v_r)v_r\Delta v_r. \tag{A1}$$

The calculated 2D image in Fig. 6(b) was constructed by the operation in Eq. (A1). In actuality, only a single centerline TOF (i.e., for $v_r=0$) is needed to obtain $P(v)$. The second method for fitting data follows from Eq. (9). A trial $P(v)$ function is chosen and $I_v(v_z)$ is calculated for individual increments of v and adding the results to obtain $I(v_z)$. Formally it is described by the operation

$$I_\alpha(v_z)=\kappa\int_0^\infty \frac{d\sigma}{d\Omega_\alpha}\frac{P(v)}{v}\,\eta_v(v_r)dv$$

$$=\frac{\kappa}{v}\frac{d\sigma}{d\Omega_\alpha}\sum_v P(v)\,\eta_v(v_r)\Delta v \tag{A2}$$

which is similar to Eq. (9) except that we have used a generalized function rather than a step function for the radial resolution (aperture function).

An important simplication occurs when $\beta=0$ and $P(v)$ can be described by a Maxwell–Boltzmann distributions (i.e., $P(v)dv=\exp\{-v^2/\sigma_v^2\}v^2\,dv$, where σ_v is the Gaussian width). Equation (9) becomes

$$I(v_z)=\kappa\int_{v_{\min}}^{v_{\max}} e^{-v^2/\sigma_v^2}\,v\,dv$$

$$=\frac{\kappa\sigma_v^2}{2}\,e^{-v_z^2/\sigma_v^2}[1-e^{-v_r^2/\sigma_v^2}]. \tag{A3}$$

The limits of integration define the allowable values of v that contribute to $I(v_z)$ and are given by $v_z\leqslant v\leqslant(v_z^2+v_r^2)^{1/2}$. Equation (A3) describes the interesting property of isotropic Maxwell–Boltzmann distributions that any 1D cylindrical slice of the 3D Gaussian distribution gives the same shaped curve for $I(v_z)$. The relation $v_z^2I(v_z)\propto P(v)$ is, therefore, equally valid for 1D projection and core sampling conditions.

[1] A. H. Zewail, J. Phys. Chem. **97**, 12427 (1993), and references therein.
[2] *Femtosecond Chemistry*, edited by J. Manz and L. Woeste (VCH, New York, 1995), and references therein.
[3] D. Imre, J. L. Kinsey, A. Sinha, and J. Krenos, J. Phys. Chem. **88**, 3956 (1984).
[4] *Molecular Photodissociation Dynamics*, edited by M. N. R. Ashfold and J. E. Baggott (Royals Society of Chemistry, London, 1987), and references therein.
[5] R. N. Dixon, Acc. Chem. Res. **24**, 16 (1991); P. L. Houston, J. Phys. Chem. **91**, 5378 (1987); J. P. Simon *ibid*. **91**, 5388 (1987).
[6] R. Schinke, *Photodissociation Dynamics* (Cambridge U.P., New York, 1993), and references therein.
[7] D. G. Truhlar, *Potential Energy Surfaces and Dynamics Calculations* (Plenum, New York, 1981), and references therein.
[8] S. J. Riley and K. R. Wilson, Faraday Discuss. Chem. Soc. **53**, 132 (1972).
[9] Y. T. Lee, Chem. Scr. **27**, 215 (1987).
[10] J. Krautwald, L. Schnieder, K. H. Welge, and M. N. R. Ashfold, Faraday Discuss. Chem. Soc. **82**, 99 (1986).
[11] L. Schenieder, W. Maier, K. H. Welge, M. N. R. Ashfold, and C. M. Western, J. Chem. Phys. **92**, 7027 (1990).
[12] J. Segall, Y. Wen, R. Lavi, R. Singer, and C. Wittig, J. Phys. Chem. **95**, 8078 (1991).
[13] R. Vasudev, R. N. Zare, and R. N. Dixon, J. Chem. Phys. **80**, 4863 (1984); R. N. Dixon, J. Chem. Phys. **85**, 1866 (1986).
[14] I. Nadler, D. Mahgerefteh, H. Reisler, and C. Wittig, J. Chem. Phys. **82**, 3885 (1985).
[15] Z. Xu, B. Koplitz, and C. Wittig, J. Chem. Phys. **90**, 2692 (1989).
[16] R. Ogorzalek Loo, H.-P. Haerri, G. E. Hall, and P. L. Houston, J. Chem. Phys. **90**, 4222 (1989); R. Ogorzalek Loo, G. E. Hall, H.-P. Haerri, and P. L. Houston, J. Phys. Chem. **92**, 5 (1988).
[17] H. J. Hwang, J. Griffiths, and M. A. El-Sayed, Int. J. Mass Spectrom. Ion Proc. **131**, 265 (1994), and references therein.
[18] M. Mons and I. Dimicoli, J. Chem. Phys. **90**, 4037 (1989).
[19] W. R. Simpson, A. J. Orr-Ewing, T. P. Rakitzis, S. A. Kandel, and R. N. Zare, J. Chem. Phys. **103**, 7299 (1995).
[20] T. Baumert, S. Pedersen, and A. H. Zewail, J. Phys. Chem. **97**, 12447 (1993).
[21] D. W. Chandler and P. L. Houston, J. Chem. Phys. **87**, 1445 (1987).
[22] A. J. R. Heck and D. W. Chandler, Annu. Rev. Phys. Chem. **46**, 335 (1995).
[23] T. N. Kitsopoulos, M. A. Buntine, D. P. Baldwin, R. N. Zare, and D. W. Chandler, Science **260**, 1605 (1993); L. S. Buntuyan, A. G. Suits, P. L. Houston, and B. J. Whitaker, J. Phys. Chem. **97**, 6342 (1993).
[24] T. Kinugawa and T. Arikawa, J. Chem. Phys. **96**, 4801 (1992).
[25] K. Tonokura and T. Suzuki, Chem. Phys. Lett. **224**, 1 (1994).
[26] K.-M. Chen, Chem. Phys. Lett. **198**, 288 (1992).
[27] G. Gruenefeld and P. Andresen, Chem. Phys. Lett. **208**, 369 (1993).
[28] R. A. Hertz and J. A. Syage, J. Chem. Phys. **100**, 9265 (1994).
[29] J. A. Syage, J. Phys. Chem. **99**, 16530 (1995).
[30] J. A. Syage, Chem. Phys. Lett. **245**, 605 (1995); J. A. Syage, Chem. Phys. in press (1996).
[31] W. C. Wiley and I. H. McLaren, Rev. Sci. Instrum. **26**, 1150 (1955).
[32] R. K. Sparks, K. Shobatake, L. R. Carlson, and Y. T. Lee, J. Chem. Phys. **75**, 3838 (1981).
[33] G. N. A. van Veen, T. Baller, A. E. de Vries, and N. J. A. van Veen, Chem. Phys. **87**, 405 (1984); M. D. Barry and P. A. Gorry, Mol. Phys. **52**, 461 (1984).
[34] R. S. Mulliken, J. Chem. Phys. **8**, 382 (1940); **3**, 513 (1935).
[35] M. Shapiro, J. Phys. Chem. **90**, 3644 (1986).
[36] M. Tadjeddine, J. P. Flament, and C. Teichteil, Chem. Phys. **118**, 45 (1987).
[37] S. K. Gray and M. S. Child, Mol. Phys. **51**, 189 (1984).
[38] S. M. Penn, C. C. Hayden, K. J. Carlson Muyskens, and F. F. Crim, J. Chem. Phys. **89**, 2909 (1988).
[39] J. F. Black and I. Powis, Chem. Phys. **125**, 375 (1988).
[40] J. L. Knee, L. R. Khundkar, and A. H. Zewail, J. Chem. Phys. **83**, 1996 (1985).
[41] K. Q. Lao, M. D. Person, P. Xayariboun, and L. J. Butler, J. Chem. Phys. **92**, 823 (1990).
[42] Y. Jiang, M. R. Giorgi-Arnazzi, and R. B. Berstein, J. Phys. Chem. **106**, 171 (1986).

[43] A. Gedanken and M. D. Rowe, Chem. Phys. Lett. **34**, 39 (1975); **137**, 462 (1987).
[44] S. J. Riley and K. R. Wilson, Faraday Discuss. Chem. Soc. **53**, 132 (1972).
[45] W. P. Hess, S. J. Kohler, H. K. Haugen, and S. R. Leone, J. Chem. Phys. **84**, 2143 (1986).
[46] F. Hunter and K. S., Chem. Phys. Lett. **58**, 291 (1978).
[47] R. L. Miller, A. G. Suits, P. L. Houston, R. Toumi, J. A. Mack, and A. M. Wodtke, Science **265**, 1831 (1994).
[48] J. M. Price, J. A. Mack, C. A. Rogaski, and A. M. Wodtke, Chem. Phys. **175**, 83 (1993).
[49] C. A. Rogaski, J. M. Price, J. A. Mack, and A. M. Wodtke, Goephys. Res. Lett. **20**, 2885 (1995).
[50] J. Eluszkiewicz and M. Allen, J. Geophys. Lett. **98**, 1069 (1993).
[51] R. P. Wayne, J. Geophys. Res. **98**, 13119 (1993); Atmos. Environ. **21**, 1683 (1987), and references therein.
[52] C. E. Fairchild, E. J. Stone, and G. M. Lawrence, J. Chem. Phys. **69**, 3632 (1978).
[53] R. K. Sparks, L. R. Carlson, K. Shobatake, M. L. Kowalczyk, and Y. T. Lee, J. Chem. Phys. **72**, 1401 (1980).
[54] T. Kinugawa, T. Sato, T. Arikawa, Y. Matsumi, and M. Kawasaki, J. Chem. Phys. **93**, 3289 (1990).
[55] S. M. Shamsuddin, Y. Inagaki, Y. Matsumi, and M. Kawasaki, Can. J. Chem. **72**, 637 (1994).
[56] D. Stranges, X. Yang, J. D. Chesko, and A. G. Suits, J. Chem. Phys. **102**, 6067 (1995).
[57] T. Bergmann, T. P. Martin, and H. Schaber, Rev. Sci. Instrum. **60**, 347 (1989).
[58] J. E. Pollard, D. A. Lichtin, S. W. Janson, and R. B. Cohen, Rev. Sci. Instrum. **60**, 3171 (1989); **61**, 3134 (1990).
[59] A. Garcia-Vela and R. B. Gerber, J. Chem. Phys. **98**, 427 (1993).
[60] T. Schroeder, R. Schinke, M. Mandziuk, and Z. Bacic, J. Chem. Phys. **100**, 7239 (1994).